PNAS RESEARCH ARTICLE | PHYSICS

# Superradiant Thomson scattering from graphite in the extreme ultraviolet

Claudia Fasolato[a,b,1], Elena Stellino[a], Emiliano Principi[c], Riccardo Mincigrucci[c], Jacopo Stefano Pelli-Cresi[c], Laura Foglia[c], Paolo Postorino[d], Francesco Sacchetti[a,e], and Caterina Petrillo[a,f]

Edited by Siegfried H. Glenzer, SLAC National Accelerator Laboratory, Menlo Park, CA; received December 16, 2022; accepted December 5, 2023 by Editorial Board Member Bernard F. Schutz

**We study the Thomson scattering from highly oriented pyrolitic graphite excited by the extreme ultraviolet, coherent pulses of FERMI free electron laser (FEL). An apparent nonlinear behavior is observed and fully described in terms of the coherent nature of both exciting FEL beam and scattered radiation, producing an intensity-dependent enhancement of the Thomson scattering cross-section. The process resembles Dicke's superradiant phenomenon and is thus interpreted as the observation of superradiant Thomson scattering. The process also triggers the creation of coherent, low-$q$ ($< 0.3$ Å$^{-1}$), low energy phonons. The experimental data and analysis provide quantitative information on the sample characteristics, absorption, scattering factor, and coherent phonon energies and populations and open the route for the investigation of the deep nature of complex materials.**

superradiant scattering | X-ray phonon scattering | free electron laser

Radiation–matter interaction can be generally described using low-order perturbation theory, due to the relatively small coupling constant $\alpha = e^2/\hbar c \simeq 1/137$ (1, 2). That approximation is considered accurate, in the non-relativistic range, when the incident and scattered radiation can be represented as singly occupied photon states. That condition breaks down in exotic environments, e.g., high energy density astrophysical objects, like pulsars (3, 4), where the radiation states take the form of coherent states with large ($>1$) average occupation numbers. A (Compton) scattering theory involving coherent radiation states has been long available (5), but specific applications to laboratory scattering experiments do not exist yet. In the last decades, free electron lasers (FELs) opened new routes to study different states of matter (6–8), extending Thomson scattering at short wavelengths (0.05 to 0.2 nm) to the study of low $Z$ elements out of equilibrium (9–13) and providing direct access to the evolution of low energy, coherent excitations in matter in the pump–probe scheme (14–19).

Here, we exploit the high degree of coherence, ensured by the seeded nature of the FEL at FERMI facility (Trieste, Italy), and its high power density ($\approx$ TW/cm$^2$) in a small space-time range ($\lesssim 10^{-6}$ cm$^2$ $\times$ $10^2$ fs) (19, 20), to explore the nonlinearities in radiation–matter interaction by a properly designed scattering experiment, where coherence in quantum mechanics (QM) plays a crucial role. Over the last decade, the linear response approximation was observed to break down already in transmission experiments, employing intense and short ($<$ 100 fs) extreme ultraviolet (EUV) pulses (21–23). There, the nonlinearity observed was ascribed to the abrupt FEL-induced modification of the sample state, not fundamentally affecting the probe-sample coupling. Instead, in our experiment, we observe a nonlinear amplification of the scattering cross-section which is intrinsic, i.e., not primarily associated with a FEL-modified sample state.

In detail, we observe a positive exponential dependence of the scattered intensity on the incident intensity, varying due to the intrinsic FEL emission fluctuations, and the excitation of low-energy coherent phonons in the material. That effect can be thought as belonging to the class of superradiant processes, defined by Gross and Haroche as "cooperative process(es) involving in a collective mode all the atoms of the sample" (24), leading to an enhanced production of photons with characteristic features. Here, the collective mode is a specific phonon, which couples to the incoming and outgoing photons of the scattering event. Superradiance has been initially predicted (25) and observed (26) in emission experiments, while superradiant scattering has been reported only in astrophysical contexts or analogues (27) and, at the laboratory scale, in the study of the collective excitation of cold atom condensates (28, 29). Here, we present a QM description of a superradiant scattering process from a crystal, in which phonons act as triggered collective modes.

## Significance

We present a Thomson scattering study on graphite, excited using the extreme ultraviolet (EUV) pulses (70 fs) of FERMI free electron laser in non-standard experimental conditions, for exciting photon densities and wavelength range. We observe and describe the growth of Thomson cross-section associated with the effect of quantum coherence, in line with Dicke's theory of superradiance, interpreting our observation as a Thomson superradiant scattering process. We believe this work opens the way for a deeper understanding EUV-to-X ray experiments, conducted under the extreme excitation conditions common to the frontier research at free electron lasers. It also provides fundamental insights into linear and nonlinear properties of matter excited in the EUV.

Author contributions: C.F., P.P., F.S., and C.P. designed research; C.F., E.S., E.P., R.M., J.S.P.-C., L.F., F.S., and C.P. performed research; E.P. and R.M. constructed experimental setup; C.F., E.S., and F.S. analyzed data; and C.F., E.S., P.P., F.S., and C.P. wrote the paper.

The authors declare no competing interest.

This article is a PNAS Direct Submission. S.H.G. is a guest editor invited by the Editorial Board.



[1]To whom correspondence may be addressed. Email: claudia.fasolato@cnr.it.

This article contains supporting information online at https://www.pnas.org/lookup/suppl/doi:10.1073/pnas.2221293121/-/DCSupplemental.

Published January 19, 2024.

In scattering processes, the presence of a coherent state of incoming radiation has no specific effect on the probe-sample coupling (5), while a coherent final state produces an amplification of the scattering cross-section at the lowest order of the perturbation theory. That kind of phenomenon is hardly visible in the scattering by electrons in condensed matter physics, where the final states are limited by conservation rules only, while they are more likely observed in phonon scattering, owing to the upper bound of phonon energy, limiting the number of available scattering channels. Hence, a sub-picosecond duration of the FEL probe pulse much shorter than the typical phonon lifetimes (30), yet much longer than the radiation period $\lambda_0/c \approx 0.01$ fs can trigger a coherent scattering process with a final coherent photon state in the Glauber's sense (31), resulting in the observation of a fundamentally nonlinear process. Thus, we found that superradiant scattering experiments in condensed matter allow for exploring the scattering from phonons with final coherent radiation states.

That regime is achievable by employing EUV photons (20) so that only a small fraction of the Brillouin zone (BZ) (i.e., few modes) is accessible and the nonlinear process is activated. Conveniently, in stacked 2D systems, along the unique axis, a reduced number of states in the $q-$space is sampled, and the number of scattering channels is smaller: Here, the hexagonal graphite is studied as a prototype for 2D systems. That class includes many complex and interesting materials like, for instance, the vast group of transition metal dichalcogenides (32). We will discuss how the described superradiant scattering process triggers nonthermal populations of coherent phonons at low-momentum $q$ in such systems by employing sub-picosecond coherent EUV pulses.

## Experimental Design

We carried out a Thomson scattering study on highly oriented pyrolytic graphite (HOPG) using the ≈70 fs EUV pulses of FERMI (33), beamline EIS-TIMEX (16). Two harmonics of FEL-2 configuration were employed, $\lambda_0^{(1)} = 4.08$ nm and $\lambda_0^{(2)} = 4.74$ nm, which correspond to photon energies $\simeq \pm 20$ eV around the carbon absorption K-edge ($E_K \approx 285$ eV) (34). Such wavelengths allow to access the previously unexplored region of low $q$ transfer (8, 9). The sample orientation was fixed (to keep the scattering volume constant), the HOPG c-axis forming a 65° angle with the incident beam, while the angle of detection was varied in the $\theta = 60°$ to 150° range. The sample thickness is about 1 mm; thus, the HOPG can be considered as a bulk system in the present experiment as, considering the absorption properties of the sample, surface effects account for less than 3% of the observed scattering process. The scattering geometry is sketched in Fig. 1*A*. Two FEL linear polarizations ($\epsilon_0$, s and p, perpendicular or parallel to the scattering plane) were used for both $\lambda_0$. The incident intensity $I_0$ was determined, pulse by pulse, by the photocurrent from the FEL focusing mirror, and a microchannel plate (MCP) detector measured the scattered intensity $I_{scat}$. The energy density was about 0.2 J/cm$^2$ with 1 μJ pulse. In the worst case ($\lambda_0^{(1)}$), given an absorption length of about 100 nm and the 300-eV photon energy, there is an energy release of about 0.3 eV/atom per pulse: only the accumulation of hundreds of FEL pulses could produce damage, as was directly observed. Accordingly, on each sample spot, a total of five single-shot acquisitions were collected to guarantee the minimum sample damage, by making a pulse-by-pulse statistical control and then shifting the sample by 100 μm to perform a new measurement on a pristine area. In these conditions, only the occupation number of a few, specific vibrational modes is expected to change due to the scattering event.

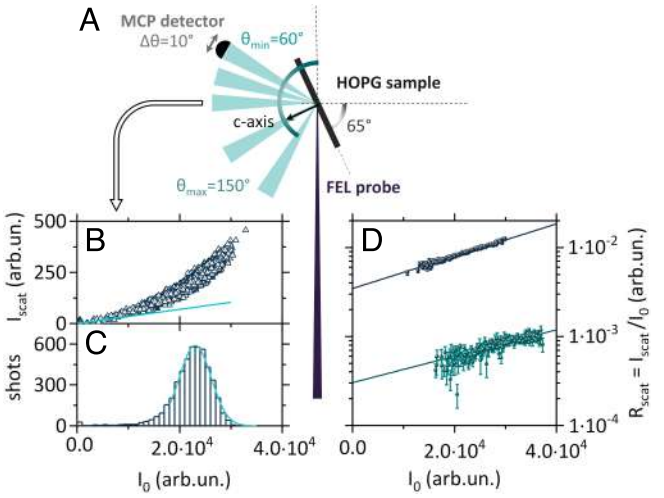


**Fig. 1.** (*A*) Experimental setup (*Top* view). The FEL beam impinges on the sample tilted by 65°. The scattered radiation is collected by the MCP, with a 10° angular opening, at variable $\theta$ (60° to 150°). (*B*) Measured scattered intensity $I_{scat}$ vs. FEL incident intensity $I_0$ per single shot, for $\lambda_0^{(1)} = 4.08$ nm, $\epsilon_0 =$ s, $\theta = 90°$. The linear plot is the trend expected assuming the cross-section as extrapolated ($I_0 \to 0$) from the fitting in panel *D* (see *SI Appendix*, Page S3, for further details). (*C*) $I_0$ histogram of data in panel (*B*) with Gaussian fitting (see text). (*D*) $R_{scat}$ vs. $I_0$ for $\lambda_0^{(1)}$ (blue dots) and $\lambda_0^{(2)}$ (cyan dots), $\epsilon_0 =$ s, $\theta = 90°$, plotted in a semi-log scale for better visualization. Notice the similar exponential relative increase and the remarkably different value at $I_0 = 0$. Data are corrected according to the statistical analysis (see text). Solid lines are single exponential fits to the data.

## Results and Discussion

**Thomson Scattering Data: Pretreatment and Observations.** Owing to the intrinsic fluctuations of the FEL (35) lasing process (see a histogram of the incident intensity $I_0$ in Fig. 1*C*), each independent dataset at given $\lambda_0, \epsilon_0, \theta$ of our experiment (Fig. 1*B*) was treated by averaging the ratio of $I_{scat}$ to the incoming $I_0$, $R_{scat}(I_0) = I_{scat}(I_0)/I_0$, over several different sample points. The average was taken in small enough intervals of $I_0$. Statistically meaningful data were obtained rejecting the $I_0$ intervals with too few (<5) data within them and (rare) fluctuations larger than twice the SDs.

In linear Thomson scattering, $R_{scat}(I_0)$ does not depend on $I_0$ resulting as an intrinsic system property, proportional to the scattering cross-section $\Sigma(\lambda_0, \epsilon_0, \theta) = \int d^2\sigma(\lambda_0, \epsilon_0, \theta)/d\Omega dE$, integrating over final energy and detector solid angle and summing the final polarizations. The observed $R_{scat}(I_0)$ vs. $I_0$, shown in Fig. 1*D*, appears far from a constant. That happens for every $\lambda_0, \epsilon_0$. We ruled out the possible experimental artifacts: a saturation of $I_0$ is not expected, and the low scattered intensity does not support a nonlinear trend of the MCP detector. Furthermore, both $I_0$ and $I_{scat}$ show Gaussian-like fluctuation distributions (see e.g., the fit to the part of the distribution in Fig. 1*C* considered statistically adequate for the $R_{scat}$ calculation and consequent analysis), thus supporting the absence of undesired anomalies. For additional details on the measurement of intensity, please refer to *SI Appendix*.

**Physical Model of the Scattering Cross-Section.** To derive useful information from the experiment, we need a model of the

Thomson cross-section in the present conditions. As it is well known, Thomson scattering originates from the coupling between electrons and the radiation field, with both electronic states and nuclear vibrations contributing (14). Thus, the final energy-integrated cross-section is the sum of the electronic $d\sigma/d\Omega|_e$ and the phononic $d\sigma/d\Omega|_{ph}$ contributions. At the first perturbative order, the cross-section is factorized into two terms: a structure factor, containing $\alpha^2$ and the effect of the system structure, and the sum of the correlation functions describing the electron and phonon dynamics (1, 2).

In the present context, initial and final radiation fields are properly described using coherent states (31) $|I\rangle$ and $|F\rangle$, where all the occupation numbers contribute with Poisson statistics (5), instead of the photon states in the Fock space, with zero or one occupation numbers. Accordingly, one can calculate the transition matrix element $\mathcal{M}_{I,F} \propto \sum_{il} \left\langle F|e^{-i(\boldsymbol{k}-\boldsymbol{k}_0)\cdot(\boldsymbol{r}_i+\boldsymbol{u}_l)}|I\right\rangle$, where $\boldsymbol{r}_i$ and $\boldsymbol{u}_l$ are the electron position and nucleus displacement operators, and $\boldsymbol{k}_0$, $\boldsymbol{k}$ are the incident and final photon wavevectors. The coherent states $|I\rangle$ and $|F\rangle$ are eigenvectors of the photon annihilation operators with complex eigenvalues $\alpha_I$ and $\alpha_F$ and average occupation numbers $n_I = |\alpha_I|^2$ and $n_F = |\alpha_F|^2$. One recovers the standard condition when $n_I \to 0$ so that the usual treatment is meaningful. The scattering cross-section becomes proportional to $n_F$ and a final coherent state is expected when $n_I$ is large and the number of final channels is small. A coherent $|F\rangle$ is not expected for $d\sigma/d\Omega|_e$, which has many open final state channels, whereas for $d\sigma/d\Omega|_{ph}$, the situation is different. In the present experiment, $\lambda_0 \approx 4$ to 5 nm; hence, the accessible volume in the reciprocal space is a small fraction of the first BZ, and only a few phonon modes, i.e., final state channels, are involved. Furthermore, a coherent initial state is present. We have:

$$\left.\frac{d\sigma}{d\Omega}\right|_{ph} = \left.\frac{d\sigma^+}{d\Omega}\right|_{ph} + \left.\frac{d\sigma^-}{d\Omega}\right|_{ph} = \frac{k}{k_0}\left[S^+_{ph}(\boldsymbol{q})\, n^+_F + S^-_{ph}(\boldsymbol{q}) n^-_F\right],$$

where we distinguish the different channels for phonon creation ($^+$) and annihilation ($^-$). $S^+_{ph}(\boldsymbol{q})$ and $S^-_{ph}(\boldsymbol{q})$ are the phonon static structure factors, i.e., the integrals of the dynamic structure factors corresponding to $n^+_F$ and $n^-_F$, respectively:

$$S^+_{ph}(\boldsymbol{q},\omega) = N_{\boldsymbol{q}j} C(\boldsymbol{q}j)(\tilde{n}_{\boldsymbol{q}j}+1)\delta(\omega-\omega_{\boldsymbol{q}j})\,\delta(\boldsymbol{k}o-\boldsymbol{k}+\boldsymbol{q})$$
$$S^-_{ph}(\boldsymbol{q},\omega) = N_{\boldsymbol{q}j} C(\boldsymbol{q}j)(\tilde{n}_{\boldsymbol{q}j})\delta(\omega+\omega_{\boldsymbol{q}j})\,\delta(\boldsymbol{k}o-\boldsymbol{k}-\boldsymbol{q}).$$

Here, $C(\boldsymbol{q}j) = \left|\boldsymbol{F}_{\boldsymbol{q}j}\cdot\boldsymbol{q}\right|^2 P(\boldsymbol{\epsilon},\boldsymbol{\epsilon}_0)/(2M\omega_{\boldsymbol{q}j})$ with $M$ atomic mass, and $P(\boldsymbol{\epsilon},\boldsymbol{\epsilon}_0)$ accounts for the effect of the beam polarizations. $\boldsymbol{F}_{\boldsymbol{q}j}$, $\hbar\omega_{\boldsymbol{q}j}$, and $\tilde{n}_{\boldsymbol{q}j}$ are the structure factor, energy and occupation number of the phonon state of momentum $\boldsymbol{q}$ in the $j$-th branch. $N_{\boldsymbol{q}j}$ is the number of normal modes in the scattering volume defined by the scattering solid angle. Considering that $\omega_{\boldsymbol{q}j} \ll ck_0$, we can safely set in the following $k/k_0 = 1$. As routine, the scattering equations are derived under the assumption that the incoming beam total energy is much higher than that of the scattered beam. Two effects contribute to reducing the incoming beam intensity, namely the scattering itself and the absorption. The reduction due to the scattering is related to the contribution of all possible scattering processes and results in a rather complex equation. This contribution is not negligible when the rate $dn/dt \approx n/T_p$, $T_p$ being the pulse duration. Therefore, in the present observation, this contribution is assumed to be small enough in order to neglect it. When these effects are included, a threshold for the exponential growth could be present.

Finally, the scattered photon rate, $dn/dt = dn^+/dt + dn^-/dt$, is evaluated considering a time-dependent incident intensity, proportional to the measured $I_0$ through an unknown efficiency $K_0$, $n_0 f(t) = K_0\, I_0 f(t)$, with $\int_{-\infty}^{+\infty} f(t)dt = 1$:

$$\begin{cases} \dfrac{dn^+(t)}{dt} = n_0 f(t)\, N_{\boldsymbol{q}j}\, C(\boldsymbol{q}j)[\tilde{n}_{\boldsymbol{q}j}+1]n^+(t) \\ \dfrac{dn^-(t)}{dt} = n_0 f(t)\, N_{\boldsymbol{q}j}\, C(\boldsymbol{q}j)\tilde{n}_{\boldsymbol{q}j}(t)n^-(t), \end{cases} \quad [1]$$

where $\tilde{n}_{\boldsymbol{q}j}(t) = \tilde{n}_B(\hbar\omega_{\boldsymbol{q}j}) + n^+(t) - n^-(t)$ is the time-dependent occupation number of the $\boldsymbol{q}j$ phonon mode and $\tilde{n}_B(\hbar\omega_{\boldsymbol{q}j})$ is its Bose occupation number. In Eq. **1**, it is not specified that the quantum numbers associated with creation and annihilation have wavenumbers that are slightly different (negligibly, since $\omega_{\boldsymbol{q}j} \ll ck_0$). Both channels contribute to $I_{scat}$, as do all the modes within the detector solid angle.

Notice two important points: first, since QM governs the processes, the rate of phonon creation is higher than that of annihilation, $n^+(t) - n^-(t) > 0$ and, consequently, $\tilde{n}_{\boldsymbol{q}j}(t) > \tilde{n}_B(\hbar\omega_{\boldsymbol{q}j})$ and, second, the presence of $N_{\boldsymbol{q}j}$ times $C(\boldsymbol{q}j)$ will have a determining role in the exponential growth of the ratio of scattered to incident intensities. The well-known detailed balance property, at thermal equilibrium, is also a consequence of the fact that $a$ and $a^+$ do not commute.

**Experimental Data Fitting.** In order to use the model to describe the experimental data, we recall that i) $I_{scat}$ is measured within the collection time of the MCP detector ($t_c \approx 1$ to 2 ns) and ii) the creation and annihilation processes cannot be distinguished (the detection is energy integrated). Accordingly, we take:

$$R_{scat} = \frac{I_{scat}}{I_0} = \frac{K_0}{K}\, lim_{t\to\infty}\left[\frac{n(t)}{n_0}\right],$$

with the (unknown) proportionality constant related to the detection efficiencies $K_0$ and $K$. To model $\lim_{t\to\infty} n(t)/n_0$, we use the analytical solution for the ratio $n^+(t)/n^-(t)$, with integration constant from the system thermodynamic equilibrium state and $g(t) = \int_{-\infty}^{t} dt' f(t')$. Fixing a time $t_f > T_p$, we get:

$$\rho(t_f) = \frac{n^+(t_f)}{n^-(t_f)} = \frac{\tilde{n}_{\boldsymbol{q}j}(t_f)+1}{\tilde{n}_{\boldsymbol{q}j}(t_f)}\, \exp\left[n_0 N_{\boldsymbol{q}j} C(\boldsymbol{q}j) g(t_f)\right]. \quad [2]$$

From Eqs. **1** and **2**, we obtain the following relation, describing the exponential growth of the scattered to incoming intensity ratio. This exponential growth resembles the result of ref. 28 where, in a different context, it is found a similar behavior for the quasi-elastic scattering of light from a Bose–Einstein condensate, the common features being the small number of condensed matter states and the exponential growth.

$$\frac{n(t_f)}{n_0} \simeq C(\boldsymbol{q}j)[2\tilde{n}_B(\hbar\omega_{\boldsymbol{q}j})+1] \cdot \exp\left[\frac{1}{2} n_0 N_{\boldsymbol{q}j} C(\boldsymbol{q}j)\left(\tilde{n}_{\boldsymbol{q}j}(t_f) + \frac{\rho(t_f)}{\rho(t_f)+1}\right)\right]. \quad [3]$$

The factor $C(\boldsymbol{q}j)$ is larger for low energy longitudinal modes, and it is zero for transverse modes because the structure factor is

proportional to the projection of the eigenvector on $\boldsymbol{q}$. In X-ray scattering in the 0.1-nm wavelength region, this contribution is fairly simple because it is directly obtained from the phonon eigenvectors tightly related to the nuclear crystal symmetry. In the case of the scattering at relatively low energy, and at an energy close to an absorption edge, $\boldsymbol{F_{qj}} \cdot \boldsymbol{q}$ contains much more information because the structure factor vector $\boldsymbol{F_{qj}}$ depends on both the ground and excited electron states. That makes the experiments more demanding but also provides a means for the investigation of complex materials and better validation of the theoretical estimates of the real and imaginary parts of the scattering factors. In the present case one can assume that, among the twelve modes of HOPG at each $\boldsymbol{q}$, the only ones contributing significantly are the longitudinal acoustic mode (LA, $\omega_{\boldsymbol{qj}} \simeq c_l(\hat{\boldsymbol{q}})q$) and the lowest energy longitudinal optic mode (LO, $\omega_{\boldsymbol{qj}} \approx$ const.) (36–38). The LA dispersion is known to be strongly anisotropic as the sound velocity $c_l$ is $c_l^{(c)}$ = 2.38 meV nm = 3,620 m/s along the unique axis and $c_l^{(a)}$ = 17.1 meV nm = 25,900 m/s on the hexagonal plane, with negligible direction dependence (39). Notice that the dependence of $c_l(\hat{q})$ on $\hat{q}$ is unknown when its direction is intermediate between the hexagonal plane and the hexagonal axis. Also notice that in $\tilde{n}_{\boldsymbol{qj}}(t)$, we neglect the effect of the finite phonon lifetime ($\gg$ 1 ps from the measured lineshape of the LA and LO phonon modes (36, 38)) which is much longer than the incident pulse $f(t)$ duration ($\approx$ 70 fs).

As a preliminary test of the model, in Fig. 1*D*, we show a single exponential fitting to the $R_{scat}$ data. The fit is adequate in the whole $I_0$ range explored (almost a factor of two) for both wavelengths. Besides the expected exponential trend, the most striking feature in Fig. 1*D* is the change of $R_{scat}$ on varying $\lambda_0$. A scale factor of 10 is needed to make $R_{scat}$ at $\lambda_0^{(2)}$ of the same order as that at $\lambda_0^{(1)}$. The energy dependence of $R_{scat}$ is related to some relevant physical parameters: namely, the carbon scattering factor $|f_s(\lambda_0)|^2$, the intensity reduction due to absorption, proportional to $1/\mu(\lambda_0)$, and the sampled region in the BZ $V_{scat}(\lambda_0)$, so that $R_{scat} \propto |f_s|^2 V_{scat}/\mu$. In *SI Appendix*, Page S2, we discuss how the possible assessments a priori of the energy dependence of $R_{scat}$ are characterized by a limited accuracy. We here demonstrate that the present investigation can provide solid quantitative information on the above-mentioned physical quantities, otherwise hardly accessible experimentally.

For a quantitative analysis, a fitting function to the $R_{scat}$ data is elaborated. Since non-linear fitting procedures can produce apparently good results when several correlated parameters are present, we made proper approximations to reduce the number of free parameters. We start from the calculation of $S_{ph}(\boldsymbol{q})$ for the LA and LO phonon modes. We add to it the low-$q$ prescription $S_e(q) \propto (\hbar/2m\omega_p)q^2$, $m$ being the electron mass and $\omega_p$ the plasma frequency (40), fixed by comparing to the free atom contribution. Since, as discussed above, the intensities are measured in arbitrary units, we rescale these contributions using proper scale factors for $I_0$ and for $I_{scat}/I_0$ from the two phonon modes; the electronic contribution is also rescaled accordingly. Since Eq. **3** contains a time-dependent phonon occupation number, we can use $\tilde{n}_{\boldsymbol{qj}}(t) - \tilde{n}_B(\hbar\omega_{\boldsymbol{qj}}) = n^+(t) - n^-(t)$ to describe its mild growth, because from Eqs. **1** and **2**, a closed form can be derived,

$$\tilde{n}_{\boldsymbol{qj}}(t) = \frac{\tilde{n}_B(\hbar\omega_{\boldsymbol{qj}})\, F_g(t)}{1 - n_0 N_{\boldsymbol{qj}} \int_{-\infty}^{t} f(\tau) F_g(\tau) d\tau} \qquad [4]$$

with $F_g(t) = \exp[n_0 N_{\boldsymbol{qj}} C(\boldsymbol{qj}) \int_{-\infty}^{t} f(\tau) r(\tau) d\tau]$, where we defined $r(t) = \rho(t)/[\rho(t) - 1]$. The fit was thus performed using the following expression:

$$R_{scat} = \sum_{j=1}^{2} A_j \frac{q^2}{\hbar\omega_{\boldsymbol{qj}}} [2\tilde{n}_B(\hbar\omega_{\boldsymbol{qj}}) + 1] \cdot \exp\left\{ B_e I_0 A_j \left[ \tilde{n}_{\boldsymbol{qj}} + \frac{\rho(t_f)}{\rho(t_f) + 1} \right] \right\} + A_e A_2\, q^2\, |\epsilon \cdot \epsilon_{\mathbf{0}}|^2, \qquad [5]$$

where $j = 1$ and $j = 2$ refer to longitudinal acoustic and optical modes, respectively, and $A_e$ is a normalization constant used to evaluate the (small and fixed) electron scattering contribution, as described above. The two functions $\rho(t_f)$ and $\tilde{n}_{\boldsymbol{qj}}(t)$ are properly adapted from Eqs. **2** and **4** making the following substitution, which allows for a numerical determination: $n_0 N_{\boldsymbol{qj}} C(\boldsymbol{qj}) \Rightarrow I_0 B_e A_j$, and performing numerically the various time integrations in Eq. **4** in the range $[-t_f, +t_f]$. For each phonon mode,

$$A_j = \frac{K}{K_0} \cdot C(\boldsymbol{qj})[2\tilde{n}_B(\hbar\omega_{\boldsymbol{qj}}) + 1],$$

where $K$ and $K_0$ are the two efficiency constants $K = n(t_f)/I_{scat}$ and $K_0 = n_0/I_0$, while the common growing constant $B_e = N_{\boldsymbol{qj}} K_0$ is the same for all phonon modes. We adopted the phonon dispersion measured in refs. 36 and 38 since a much larger set of data would be needed to take the phonon energies as free parameters. An additional parameter was adopted to describe the (unknown) $c_l(\hat{\boldsymbol{q}})$ change with $\boldsymbol{q}$ direction in terms of a smooth function, connecting the experimentally determined $c_l$ values along the high symmetry directions as asymptotic values. This model well fitted each dataset, typically about 600 experimental points, at four $\lambda_0$, $\epsilon_0$ configurations using only three free parameters ($A_1$, $A_2$, $B_e$), dependent on the wavelength and polarization, plus just one fixed parameter to describe the $c_l$ anisotropy (see *SI Appendix*, Page S4, for further discussion). The anisotropy parameter, useful to describe this large body of data and depending on the sample characteristics only, strongly supports the present superradiant model of the coherent radiation scattering: indeed, a possible change in the sample state, produced by the incoming radiation, could not be described using a single parameter. No $q$ dependence was assumed for the phonon structure factor, a choice suggested by the small $q$ range, which is confined well within about 1/3 of the BZ width. Further details on the angular dependence of the scattering data are available in *SI Appendix*, Page S5.

**Scattering Amplitudes, Phonon Dispersion, and Coherent Phonon Population.** The experimental $R_{scat}$ as a function of $\theta$ and $I_0$ is shown in Fig. 2, where the good agreement with the model is evident. Several quantitative information can be extracted by data fitting and will be described in the following, along with considerations, based on available data on HOPG, that strongly support our analysis and interpretation.

The first very important result is the ratio of the growth coefficients $B_e \propto N_{\boldsymbol{qj}} \propto 1/\mu$ at 4.74 nm to that at 4.08 nm, $b_e = B_e(\lambda_0^{(2)})/B_e(\lambda_0^{(1)})$. It is found $b_{e,\mathrm{p}} = 13.64 \pm 0.60$ and $b_{e,\mathrm{s}} = 15.17 \pm 0.76$ with vertical and horizontal incoming polarization, respectively. These experimental results are close to the available estimate of the ratio of the linear absorption coefficients equal to 16.7 from the free atom theory (41) and

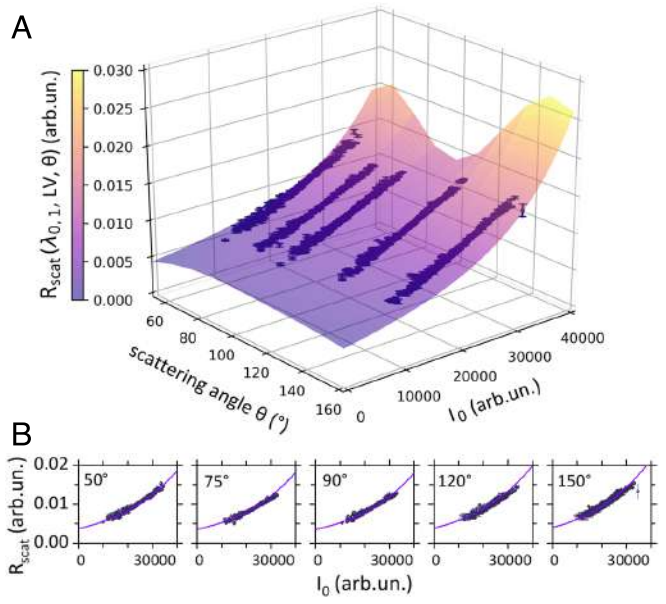


**Fig. 2.** (*A*) $R_{scat}$ vs. $I_0$ at different $\theta$ (thus, $\boldsymbol{q}$) for $\lambda_0^{(1)} = 4.08$ nm, $\epsilon_0 =$ s. Blue dots: experimental data; surface: data fitting. (*B*) Plots of data and fitting function shown in panel (*A*) for the specific, sampled scattering angles. Similar results are obtained for all the other $(\lambda_0, \epsilon_0)$ datasets.

8.1 from the experimental trends extrapolated from ref. 34; for further details, see *SI Appendix*, Fig. S1 and related comments. That result corroborates the model and introduces an approach for a quantitative determination of $\mu$ in bulk materials in this EUV or soft X-ray range.

The second quantitative result is the ratio of the amplitude coefficients $A$ at the two wavelengths, which contains $C(\boldsymbol{qj})$ and thus information on the phonon structure factor (42), for the acoustic and optical modes. The ratios, calculated for both phonons at s and p polarization, give us values close to each other and of the order of 10 (Table 1), providing quantitative indication of the strong wavelength dependence of the scattering factor and polarization factor. On the other side, we find that the ratios of the $A$ coefficients at s and p polarization, calculated for both phonons at $\lambda_0^{(1)}$ and $\lambda_0^{(2)}$, are significantly closer to unit (Table 2), indicating a rather small polarization effect on the amplitudes of the two modes. We recall that at photon energy close to the absorption edge also the polarization dependence of the scattering factors shows an energy dependence (43). It is relevant to notice that the present study can open the door to the determination of both real and imaginary parts of $f_s(\lambda_0)$ in complex materials like graphite. Considering the difficulty of the absolute determination of the linear absorption coefficient by transmission experiments, and of the scattering factors by both experiments and theory, the observed effect opens ways to the study of not only coherent radiation processes

**Table 1. Ratios of the amplitude coefficients *A* at $\lambda_0^{(1)}$ and $\lambda_0^{(2)}$ calculated for optic and acoustic phonons (1,2) at s and p polarization**

| | |
|---|---|
| $A_{1,p}(\lambda_0^{(1)})/A_{1,p}(\lambda_0^{(2)})$ | $11.10 \pm 0.26$ |
| $A_{2,p}(\lambda_0^{(1)})/A_{2,p}(\lambda_0^{(2)})$ | $11.82 \pm 0.27$ |
| $A_{1,s}(\lambda_0^{(1)})/A_{1,s}(\lambda_0^{(2)})$ | $11.77 \pm 0.29$ |
| $A_{2,s}(\lambda_0^{(1)})/A_{2,s}(\lambda_0^{(2)})$ | $8.60 \pm 0.24$ |

**Table 2. Ratios of the amplitude coefficients *A* at the two polarization s and p calculated for optic and acoustic phonons (1,2) at $\lambda_0^{(1)}$ and $\lambda_0^{(2)}$**

| | |
|---|---|
| $A_{1,p}(\lambda_0^{(1)})/A_{1,s}(\lambda_0^{(1)})$ | $0.7917 \pm 0.0076$ |
| $A_{2,p}(\lambda_0^{(1)})/A_{2,s}(\lambda_0^{(1)})$ | $0.7606 \pm 0.0090$ |
| $A_{1,p}(\lambda_0^{(2)})/A_{1,s}(\lambda_0^{(2)})$ | $0.840 \pm 0.027$ |
| $A_{2,p}(\lambda_0^{(2)})/A_{2,s}(\lambda_0^{(2)})$ | $0.553 \pm 0.019$ |

but also fundamental, and hardly accessible, material properties. Notably, when coherence effects are observed, the information on $f_s$ is contained within both the multiplying coefficient and the exponent of the trend in Eq. **3**, thus providing a more solid experimental estimate of the scattering factor, also considering that the growth coefficient $B_e$ is common to all the phonon modes involved.

It is remarkable that, while the scattered intensity is much lower below the absorption edge, the exponential growth as a function of the incoming intensity, and hence the effect of the coherence, remain similar. Indeed, the exponent factors, proportional to the product of $A$ and $B_e$, are negligibly reduced ($< 20\%$) at $\lambda_0^{(2)}$ in all the conditions explored. That is in agreement with the description of Eq. **3** and with what is readily observed from the trends in Fig. 1*D*.

From the extrapolation of $R_{scat}$ at $I_0 \to 0$, we infer that the amplitude of $S_{ph}(\boldsymbol{q})$ has a small angular dependence. That occurs because the strong anisotropy of $c_l(\hat{\boldsymbol{q}})$ (see the LA phonon dispersion in Fig. 3, discussed below) produces a decrease of the scattering contribution from the LA mode ($\approx 1/12$) at growing $\theta$, which is compensated by the $q^2$ increase of the LO part ($\approx \times 5$), an effect independent of polarization and wavelength. Some tests to check for the presence of a structure factor variation suggest that this contribution is smaller than the sensitivity of the experiment, $\approx 10\%$.

The observed variation of $c_l(\hat{\boldsymbol{q}})$ is not in agreement with the trend derived from the graphite elastic constants; therefore, the system is not equivalent to an elastic solid, even if the crystal

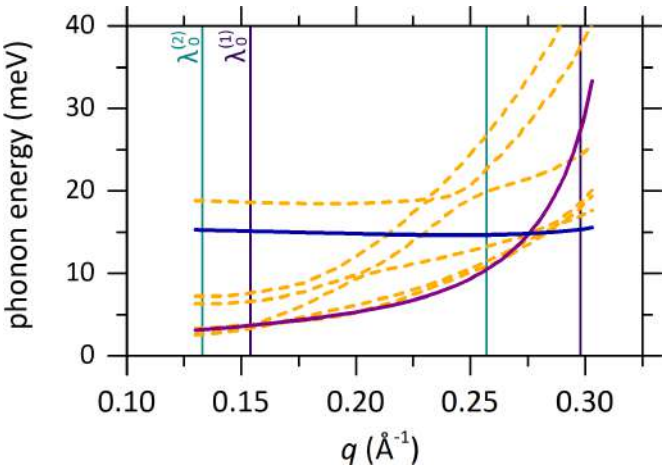


**Fig. 3.** Phonon dispersion curves (orange dashed lines) calculated by DFT in the transferred $q$ region of interest. The vertical lines mark the $q$ range explored in the experiment with $\lambda_0^{(1)}$ (blue) and $\lambda_0^{(2)}$ (cyan) excitation. The phonon dispersion is calculated performing an average over the possible crystal orientation in HOPG (obtained by rotations about the *c*-axis). The solid lines show the dispersion curves extracted by the fitting of experimental data for the low-energy acoustic (purple) and optical (blue) phonon modes.

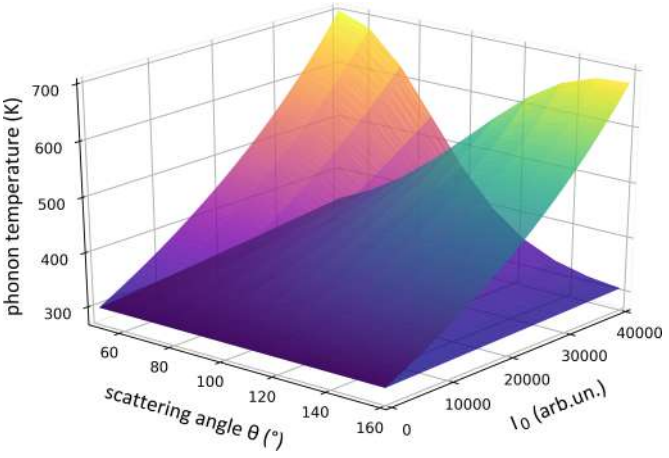


**Fig. 4.** Phonon temperature versus $I_0$ and $\theta$ calculated from the scattering-modified phonon occupation number for the LO (blue-to-yellow curve, increasing at growing $\theta$) and LA (purple-to-yellow curve) phonon modes. $\tilde{n}_{\boldsymbol{qj}}(t_f)$ is estimated by $R_{scat}$ data fitting for $\lambda_0^{(1)} = 4.08$ nm, $\epsilon_0 =$s.

symmetry is taken into account (39). To have an additional evaluation of the strong anisotropy of $c_l(\hat{\boldsymbol{q}})$ a density functional theory (DFT) calculation was performed using the exchange-correlation potential for the gradient approximation of ref. 44 and the all-electron LAPW (linearized augmented plane wave) DFT code Elk (45). The calculation has been carried out by performing an average of the dispersion relations obtained by rotation around the $c$-axis. That is necessary because of the random orientations of the small crystallites on the hexagonal plane of HOPG. In principle, only the longitudinal component of the phonon modes can contribute to the scattering in the first BZ. Considering the structure of graphite and the fact that, when the transferred momentum is not along a high symmetry direction, the phonon polarization is neither purely longitudinal nor purely transverse, all the modes tend to contribute here. In Fig. 3, the complex calculated dispersion curves are shown. A qualitative agreement is observed with the model of the fit which uses two major modes only. That result further corroborates both the presented description of the scattering data and its potential applicability in performing new kinds of investigations using more extended sets of experimental configurations. The results show that the experiment can detect the anisotropic bonding of graphene layers in HOPG, while a more extended sampling of the scattering volume is needed to thoroughly assess the aforementioned smaller contributions.

The last remark is on the final phonon state, having the characteristic of a coherent state with a specific change in the average occupation number. According to the model, quantitative information on the increase of $\tilde{n}_{\boldsymbol{qj}}(t)$ by scattering can be extracted from fitting as a by-product. In Fig. 4, we show the increase of the equivalent phonon temperature $T_{\boldsymbol{qj}}$, as estimated from $\tilde{n}_{\boldsymbol{qj}}(t_f)$. An increase of $T_{\boldsymbol{qj}}$ of the order of some hundreds K is estimated for both modes involved. The $T_{\boldsymbol{qj}}$ trends result almost independent of $\lambda_0$ , $\epsilon_0$. It is important to observe that the equivalent temperature is just a way to quantify the growth of the phonon occupation number as it is not the thermodynamic temperature. Of course, at later times, once the anharmonic phonon–phonon interaction kicks in, the energy selectively deposited in such low-$q$ hot phonon populations is redistributed among all the vibrational (as well as electronic) degrees of freedom of the system, resulting in a much lower final equilibrium temperature. The different temperatures estimated for the LA and LO phonon populations reflect the selection rules for the modes at varying scattering geometry.

## Conclusions

In conclusion, we carried out a Thomson scattering experiment on HOPG exploiting the coherent, ultrashort EUV pulses of FERMI FEL. Here, we find out the evident, crucial role of quantum coherence, as the exponential growth of the scattered intensity upon increasing incident intensity is due to the non-zero commutator of the annihilation and creation operators of the radiation final coherent state. The nonlinearity here paralleling Dicke's theory of superradiance (24, 25) represents a direct laboratory observation of coherence of the scattered EUV radiation, also promoting low-energy coherent phonons in the material, as seen in the exponential trend of $d\sigma/d\Omega|_{ph}$. The QM description of the process provides a precise picture of the data, indicating the way to obtain useful information on the specimen using a wide sampling of the available BZ volume. The present data already provide quantitative results regarding the determination of the absorption in bulk materials and the combined analysis of absorption and scattering factors in the energy region across the absorption edge, other than the study of the anisotropy of sound propagation in graphite.

Our results show that the described framework sets the basis for conceiving EUV Thomson scattering experiments, opening promising routes for material investigations. These experiments could provide information on the properties of condensed matter systems: first, they can give access to basic data, like absorption coefficient in the EUV, scattering factors in crossing the low energy absorption edges, and low-$q$ phonon dispersion curves in thin films. Second, they allow exploring exotic effects, like those produced by superradiant processes triggered by the bright and coherent EUV FEL pulses, combined with the reduced scattering volume in reciprocal space.

**Data, Materials, and Software Availability.** [txt] data have been deposited in Zenodo (46).

Author affiliations: [a]Dipartimento di Fisica e Geologia, Università di Perugia, Perugia I-06123, Italy; [b]Istituto dei Sistemi Complessi, Consiglio Nazionale delle Ricerche (CNR-ISC), Roma I-00185, Italy; [c]Elettra-Sincrotrone Trieste Società Consortile per Azioni (SCpA), Basovizza, Trieste I-34149, Italy; [d]Dipartimento di Fisica, Sapienza Università di Roma, Roma I-00185 Italy; [e]Istituto Officina dei Materiali, Consiglio Nazionale delle Ricerche (CNR-IOM), Perugia I-06123, Italy; and [f]Area Science Park, Trieste I-34149, Italy

1. W. Heitler, *The quantum theory of radiation* (Courier Corporation, 1984).
2. S. K. Sinha, Theory of inelastic X-ray scattering from condensed matter. *J. Phys.: Condens. Matter* **13**, 7511 (2001).
3. C. Kennel, F. Coroniti, Confinement of the Crab pulsar's wind by its supernova remnant. *Astrophys. J.* **283**, 694–709 (1984).
4. D. Wilson, M. Rees, Induced Compton scattering in pulsar winds. *Mon. Notic. R. Astron. Soc.* **185**, 297–304 (1978).
5. V. Moncrief, Coherent states and quantum nonperturbing measurements. *Ann. Phys.* **114**, 201–214 (1978).
6. P. Emma *et al*., First lasing and operation of an Ångstrom-wavelength free-electron laser. *Nat. Photon.* **4**, 641–647 (2010).
7. J. Rossbach, J. R. Schneider, W. Wurth, 10 years of pioneering X-ray science at the free-electron laser flash at desy. *Phys. Rep.* **808**, 1–74 (2019).
8. L. Fletcher *et al*., Ultrabright X-ray laser scattering for dynamic warm dense matter physics. *Nat. Photon.* **9**, 274–279 (2015).
9. T. Ma *et al*., X-ray scattering measurements of strong ion-ion correlations in shock-compressed aluminum. *Phys. Rev. Lett.* **110**, 065001 (2013).
10. H. Lee *et al*., X-ray Thomson-scattering measurements of density and temperature in shock-compressed beryllium. *Phys. Rev. Lett.* **102**, 115001 (2009).
11. C. Fortmann *et al*., Measurement of the adiabatic index in be compressed by counterpropagating shocks. *Phys. Rev. Lett.* **108**, 175006 (2012).

12. J. Valenzuela *et al*., Measurement of temperature and density using non-collective X-ray Thomson scattering in pulsed power produced warm dense plasmas. *Sci. Rep.* **8**, 1–8 (2018).
13. M. Bonitz, Z. A. Moldabekov, T. Ramazanov, Quantum hydrodynamics for plasmas-Quo vadis? *Phys. Plasmas* **26**, 090601 (2019).
14. S. H. Glenzer, R. Redmer, X-ray thomson scattering in high energy density plasmas. *Rev. Mod. Phys.* **81**, 1625 (2009).
15. A. Höll *et al*., Thomson scattering from near-solid density plasmas using soft X-ray free electron lasers. *High Energy Density Phys.* **3**, 120–130 (2007).
16. C. Masciovecchio *et al*., EIS: The scattering beamline at fermi. *J. Synchrot. Radiat.* **22**, 553–564 (2015).
17. M. Trigo *et al*., Fourier-transform inelastic X-ray scattering from time-and momentum-dependent phonon-phonon correlations. *Nat. Phys.* **9**, 790–794 (2013).
18. M. Kozina *et al*., Heterodyne X-ray diffuse scattering from coherent phonons. *Struct. Dyn.* **4**, 054305 (2017).
19. C. Fasolato *et al*., Ultrafast plasmon dynamics in crystalline lif triggered by intense extreme UV pulses. *Phys. Rev. Lett.* **124**, 184801 (2020).
20. M. B. Danailov *et al*., Towards jitter-free pump-probe measurements at seeded free electron laser facilities. *Opt. Expr.* **22**, 12869–12879 (2014).
21. L. Young *et al*., Femtosecond electronic response of atoms to ultra-intense X-rays. *Nature* **466**, 56–61 (2010).
22. H. Yoneda *et al*., Saturable absorption of intense hard X-rays in iron. *Nat. Commun.* **5**, 1–5 (2014).
23. A. Di Cicco *et al*., Interplay of electron heating and saturable absorption in ultrafast extreme ultraviolet transmission of condensed matter. *Phys. Rev. B* **90**, 220303 (2014).
24. M. Gross, S. Haroche, Superradiance: An essay on the theory of collective spontaneous emission. *Phys. Rep.* **93**, 301–396 (1982).
25. R. H. Dicke, Coherence in spontaneous radiation processes. *Phys. Rev.* **93**, 99 (1954).
26. M. Gross, C. Fabre, P. Pillet, S. Haroche, Observation of near-infrared Dicke superradiance on cascading transitions in atomic sodium. *Phys. Rev. Lett.* **36**, 1035 (1976).
27. T. Torres *et al*., Rotational superradiant scattering in a vortex flow. *Nat. Phys.* **13**, 833–836 (2017).
28. S. Inouye *et al*., Superradiant Rayleigh scattering from a Bose-Einstein condensate. *Science* **285**, 571–574 (1999).
29. D. Schneble *et al*., The onset of matter-wave amplification in a superradiant Bose-Einstein condensate. *Science* **300**, 475–478 (2003).
30. N. Bonini, M. Lazzeri, N. Marzari, F. Mauri, Phonon anharmonicities in graphite and graphene. *Phys. Rev. Lett.* **99**, 176802 (2007).
31. R. J. Glauber, Coherent and incoherent states of the radiation field. *Phys. Rev.* **131**, 2766 (1963).
32. S. Manzeli, D. Ovchinnikov, D. Pasquier, O. V. Yazyev, A. Kis, 2D transition metal dichalcogenides. *Nat. Rev. Mater.* **2**, 1–15 (2017).
33. E. Allaria *et al*., Highly coherent and stable pulses from the FERMI seeded free-electron laser in the extreme ultraviolet. *Nat. Photon.* **6**, 699–704 (2012).
34. J. A. Brandes *et al*., Carbon K-edge XANES spectromicroscopy of natural graphite. *Carbon* **46**, 1424–1434 (2008).
35. N. S. Mirian *et al*., Generation and measurement of intense few-femtosecond superradiant extreme-ultraviolet free-electron laser pulses. *Nat. Photon.* **15**, 523–529 (2021).
36. R. Nicklow, N. Wakabayashi, H. Smith, Lattice dynamics of pyrolytic graphite. *Phys. Rev. B* **5**, 4951 (1972).
37. J. Maultzsch, S. Reich, C. Thomsen, H. Requardt, P. Ordejón, Phonon dispersion in graphite. *Phys. Rev. Lett.* **92**, 075501 (2004).
38. M. Mohr *et al*., Phonon dispersion of graphite by inelastic X-ray scattering. *Phys. Rev. B* **76**, 035439 (2007).
39. G. Savini *et al*., Bending modes, elastic constants and mechanical stability of graphitic systems. *Carbon* **49**, 62–69 (2011).
40. D. Pines, P. Nozieres, *The theory of quantum liquids. W. A. Benjamin, inc* (New York, 1966).
41. C. T. Chantler, Theoretical form factor, attenuation, and scattering tabulation for $Z = 1$–92 from $E = 1$–10 eV to $E = 0.4$-1.0 MeV. *J. Phys. Chem. Ref. Data* **24**, 71–643 (1995).
42. B. Willis, Thermal diffuse scattering of X-rays and neutrons. *Int. Tables Crystallogr. B* **4** (1), 484–491 (2010).
43. J. C. Parker, R. Pratt, Validity of common assumptions for anomalous scattering. *Phys. Rev. A* **29**, 152 (1984).
44. J. P. Perdew *et al*., Restoring the density-gradient expansion for exchange in solids and surfaces. *Phys. Rev. Lett.* **100**, 136406 (2008).
45. Elk code (http://elk.sourceforge.net/) The exchange and correlation potential from ref. (44) was used. The intrinsic disorder of the HOPG planes about the c-axis was accounted for by calculating the dispersion relations along the $\Gamma_M$ and $\Gamma_K$ directions. Both are considered to obtain the dispersion curves in Figure 3 (2021).
46. C. Fasolato *et al*., Experimental data for "Superradiant Thomson scattering from graphite in the extreme ultraviolet". Zenodo. https://doi.org/10.5281/zenodo.7446390. Deposited 29 December 2023.